Numerical Simulation on Retreating Blade Sections of a Small UAV Helicopter in Forward Flight

Journal of Physics: Conference Series **3070** (2025) 012007 doi:10.1088/1742-6596/3070/1/012007

Numerical Simulation on Retreating Blade Sections of a Small UAV Helicopter in Forward Flight

Mohannad Y. Orabi[1*] and Mohamed Yehia Zakaria[2]

[1]PhD. Student, Aircraft Mechanics Department, Military Technical College, Cairo, Egypt
[2]Associate Professor, Head of Department of Aircraft Mechanics, Military Technical Collage, Cairo, Egypt

*E-mail: orabimohannad@windowslive.com

Abstract. This study presents computational simulations for three different spanwise locations of the retreating blade of a small UAV helicopter rotor in forward flight. The aim of the present study is to focus on its aerodynamic performance within the reversed flow regime. The results provide an aerodynamic analysis for various angles of attack at three distinct spanwise sections, examining the impact of the Reynolds number on reversed flow characteristics. The analysis emphasizes key aerodynamic parameters, including lift and drag coefficients, within the reversed flow region, comparing the effects of different angles of attack. In addition, detailed boundary layer assessments are performed through the analysis of surface pressure and skin friction coefficients. The study reveals that as the advance ratio increases, the reverse flow spreads towards the tip of the rotor's retreating blade. This results in a noticeable loss of lift, an increase in drag, and high unsteadiness, leading to unstable rotor operation. This effect is more pronounced at smaller angles of attack. However, at moderate angles, the loss of lift and the increase in drag at the tip become negligible compared to the inboard blade sections.

Keywords
CFD, Reverse Flow, Rotor Aerodynamics, UAV

Nomenclature

C_D	=	Drag coefficient
C_F	=	Skin friction coefficient
C_L	=	Lift coefficient
C_P	=	Pressure coefficient
c	=	Blade chord length
Re	=	Reynolds number
R	=	Rotor radius
r	=	Airfoil section radial location
SST	=	Shear stress transport
URANS	=	Unsteady Reynolds-averaged Navier-Stokes
V_∞	=	Forward speed
α	=	Angle of attack
μ	=	Advance ratio
Ω	=	Rotational speed
ψ	=	Blade azimuth position

1. Introduction

The phenomenon of reversed flow over retreating rotor blades is a critical aspect of helicopter aerodynamics, particularly in small Unmanned Aerial Vehicles (UAVs) operating at high advance ratios. In forward flight, the retreating blade experiences regions where the local flow reverses direction as the forward flight velocity component is greater than the velocity component due to rotor rotation. This reversed flow regime significantly influences aerodynamic forces, potentially affecting the overall performance, stability, and control characteristics of the rotor.

Historically, blade element theory has been the foundation for most theoretical research in predicting rotor performance. This method divides the rotor blade into small elements and utilizes the sectional aerodynamic forces acting on each segment, enabling the estimation of overall rotor power. Advancements in computational methods and experimental techniques enable more accurate predictions of sectional aerodynamic forces, leading to the development of sophisticated models that account for additional aerodynamic complexities, such as the reverse flow phenomenon.

Leishman proposed a simple modification for the profile power coefficient formula established using blade element theory in order to account for the reverse flow effect [1]. The proposed modification was to change the sign of both the in-plane velocity component parallel to the rotor disc plane and the sectional drag contribution in the radial and azimuthal integration used for estimating the rotor power and drag coefficients. Dayhoum et al. applied blade element theory to a rotor blade in forward flight, aiming to validate its accuracy in predicting aerodynamic loads [2–4]. By calculating lift, thrust, power, and local aerodynamic forces, the study compared theoretical normal force coefficients with experimental data from the 7A rotor at multiple radial positions. The results demonstrated a similar pattern of variation along the azimuth with notable convergence along the blade radius, confirming the reliability of the blade element theory in the preliminary design phase. More recently, Mansour et al. developed a comprehensive theoretical framework for designing a small unmanned helicopter rotor, including the selection of an optimal airfoil by comparing NACA symmetric and cambered airfoils based on sectional aerodynamic forces [5]. Additionally, they conducted computational simulations to analyze rotor performance under hovering conditions. Early experimental studies on static airfoils in reverse flow were conducted to support preliminary design efforts. Sheldahl and Klimas performed two-dimensional tests on seven symmetric airfoil sections to support analytical aerodynamic analysis of vertical axis wind turbines [6]. They reported the sectional lift and drag coefficients through the 180°angle of attack for a wide range of Reynolds numbers ranging from $Re = 10^4$ to $Re = 10^7$. This comprehensive database of angle of attack values could be utilized in analytical methods to predict rotor performance.

Critzos et al. carried out wind tunnel measurements on a NACA 0012 rectangular wing with an aspect ratio of 6, which completely spanned the low-turbulence pressure tunnel test section of the NASA Langley Research Center [7]. Just prior to stall in forward flow, a lift coefficient value of 1.3 was reached at an angle of attack of approximately 13 degrees, after which there was a steep drop in lift. In reverse flow, the airfoil attained a maximum lift coefficient of 0.8 at an angle of attack around 188 degrees, with moderately high lift maintained in the post-stall region. The results of the experimental measurements showed that at a Reynolds number of 1.8×10^6, the drag coefficient at an angle of attack of 180°was about twice that for an angle of attack of 0°. This increase in drag coefficient was consistent with the values previously measured by Pope for the NACA 0015 airfoil at a Reynolds number of 1.2×10^6 [8]. Leishman conducted wind tunnel tests on an SC1095 airfoil in reverse flow and found that the airfoil stalled earlier compared to forward flow, resulting in higher drag as the angle of attack moved away from 180° [9]. The study also revealed that drag near 180° was greater than that near 0°, due to significant bluff body separation around the airfoil's nose. Furthermore, the pitching moments about the 1/4 chord were observed to be much larger than in forward flow, as the center of lift shifted closer to the 3/4 chord point under reverse flow conditions. In developing the X2 Technology Demonstrator (X2TD), Sikorsky Aircraft Corporation made specific design modifications to the rotor blades to improve the performance in the reverse flow region [10]. Unlike the more conventional blades of the XH-59A, Sikorsky's earlier coaxial helicopter from the 1970s, the X2TD blades featured a smaller chord and lower pitch in the inboard region and utilized double-ended airfoils. Although these changes improved performance in the reverse flow region, they were likely to negatively affect hover efficiency [1]. In hover, high pitch and large chord are advantageous in the inboard sections of the blade to minimize power consumption, and the elliptical airfoil section has significantly higher drag compared to a sharp trailing-edge airfoil of similar size in forward flow. Furthermore, using double-ended airfoils in the inboard sections to optimize for reverse flow leads to more lift being generated outboard, which in turn increases rotor-induced power during hover.

Lind et al. performed wind tunnel tests on a traditional NACA 0012 airfoil and two elliptical airfoils, examining their behavior at static angles of attack through a full 360° rotation at a Reynolds number of

1.1×10^5 [11, 12]. Their results showed that the drag on the DBLN-526 elliptical airfoil was significantly higher than that on the NACA 0012 airfoil over a range of forward flow angles of attack (0°–8°). They also demonstrated that the drag on the NACA 0012 in reverse flow was more than double that in forward flow, due to flow separation over the blunt nose and sharp trailing edge.The obtained lift and drag coefficients for the NACA 0012 airfoil are compared for both forward and reverse flow conditions. Additionally, Lind et al. conducted an experimental study to investigate the effects of Reynolds number in both forward and reverse flow [13]. The study utilized two symmetric NACA airfoils at varying Reynolds numbers ranging from 3.3×10^5 to 1.0×10^6. The results indicated that, for the NACA 0012 airfoil in reverse flow, the aerodynamic loads remained largely unaffected by Reynolds number due to early flow separation. In contrast, the thicker NACA 0024 airfoil exhibited greater sensitivity to changes in Reynolds number.

Small Unmanned Aerial Vehicles have recently gained increasing interest for a wide variety of applications. In the absence of a human pilot, the issues of flight stability and performance predictability become more sophisticated. Small helicopter UAVs are a special type of UAVs in which reversed flow on blades can be a crucial aspect that has not gained the focus it deserves in the open literature. In this work, a computational analysis is presented to investigate the reversed flow region and examine the geometrical and kinematic parameters of a small helicopter rotor. The study focuses on modeling the reversed flow region at various sections of the retreating blade during forward flight.

The remainder of the paper is organized as follows. Aspects of the case study are presented in the following section followed by details of the simulation setup and validation in two separate sections. Next, results are presented and discussed. The paper wraps up with key conclusions.

2. Helicopter UAV Case Study

In the present study, the Mikado 800 mini helicopter rotor is considered as the case study. Originally, the blades were manufactured and investigated in hovering conditions by Mansour et al. [5], the rotor blade sections are analyzed to assess the impact of reversed flow on aerodynamic forces at three different radial stations on the retreating blade. The selected stations are located on the rectangular section of the rotor blade at $r/R = 0.25$, 0.5, and 0.9, corresponding to a blade azimuth position of $\psi = 270°$. The rotor is assumed to rotate counterclockwise at a constant rotational speed of 250 RPM, while the helicopter advances at a forward speed of 25 m/s. This critical assumption aligns closely with the experimental conditions reported by Hiremath et al., where a rotor advance ratio greater than unity ensures reversed flow across the entire span of the retreating blade [14]. Table 1 presents the main rotor parameters. Figure 1 shows a schematic diagram of the rotor, highlighting the selected stations analyzed in this study. The reversed flow regime on the retreating blade is represented by the red zone under the present conditions.

Table 1. Rotor main parameters.

Property	Value
Rotor radius (R)	0.9 (m)
Airfoil section	NACA 0012
Blade chord length (c)	0.066 (m)
Rotational speed (Ω)	250 (RPM)
Forward speed (V_∞)	25 m/s

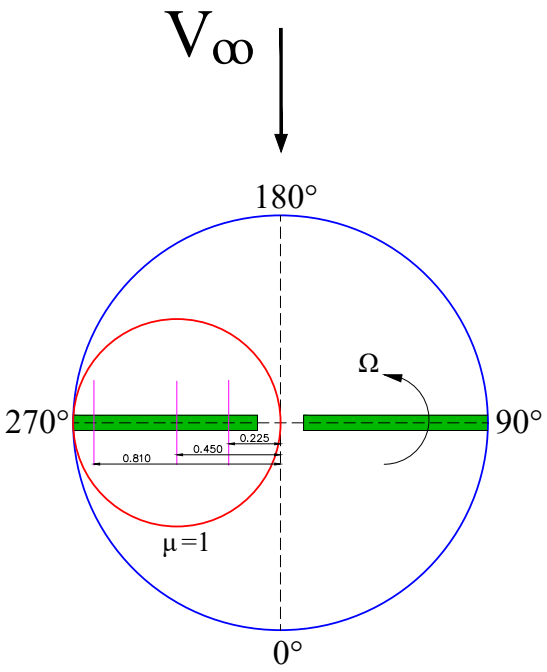

Figure 1. Selected blade sections.

3. Aerodynamic Simulations of Rotor Blade Sections

The present computational simulations are conducted considering three different static angles of attack ($\alpha = 4°$, 6°, and 8°) to demonstrate the effects of Reynolds number variation and changes in the angle of attack on reversed flow characteristics. The computational domain and mesh configuration utilized in the validation process are consistently employed for all subsequent simulations. For each station, the inlet velocity is specified to achieve the desired Reynolds number corresponding to the blade section radial location at an azimuth position of $\psi = 270°$. Since the rotor shaft tilt angle is relatively small during forward flight, the resultant relative velocity is assumed to be the difference between the forward velocity and the velocity component resulting from the rotor rotation at each section. Table 2 summarizes the detailed sections and their corresponding data.

Table 2. Selected sections data.

r/R	Ωr (m/s)	$V_\infty - \Omega r$ (m/s)	Reynolds number
0.25	5.8905	19.1095	86342
0.5	11.781	13.219	59727
0.9	21.2058	3.7942	17143

4. Computational Validation

A comprehensive framework for validating the flow over a NACA 0012 airfoil against experimental data in the reverse flow regime was provided by Orabi et al. [15]. For computational validation, a two-dimensional rectangular domain was constructed with boundary dimensions specifically optimized for external aerodynamic simulations. The airfoil model's chord length and inlet velocity were chosen to match the experimentally tested configuration, ensuring consistency with the targeted Reynolds number of 1.1×10^5 [12]. The airfoil model had a chord length of 0.07 m, which served as the characteristic length for defining all other domain dimensions. The inlet boundary was positioned 3c upstream and

designated as a velocity inlet boundary condition. The outlet boundary was located 14c downstream and defined as a pressure outlet. The upper and lower domain boundaries were placed at a distance of 5c from the airfoil and treated as symmetry boundaries. A no-slip wall condition was applied to the airfoil surface to accurately represent the physical flow characteristics. To achieve the desired angles of attack, the airfoil was rotated about a fixed point, while maintaining a constant horizontal free-stream velocity of 23 m/s. This setup ensures computational accuracy by mirroring experimental conditions and validating aerodynamic performance through numerical simulation. Figure 2 provides a schematic of the main dimensions and boundary conditions of the computational domain.

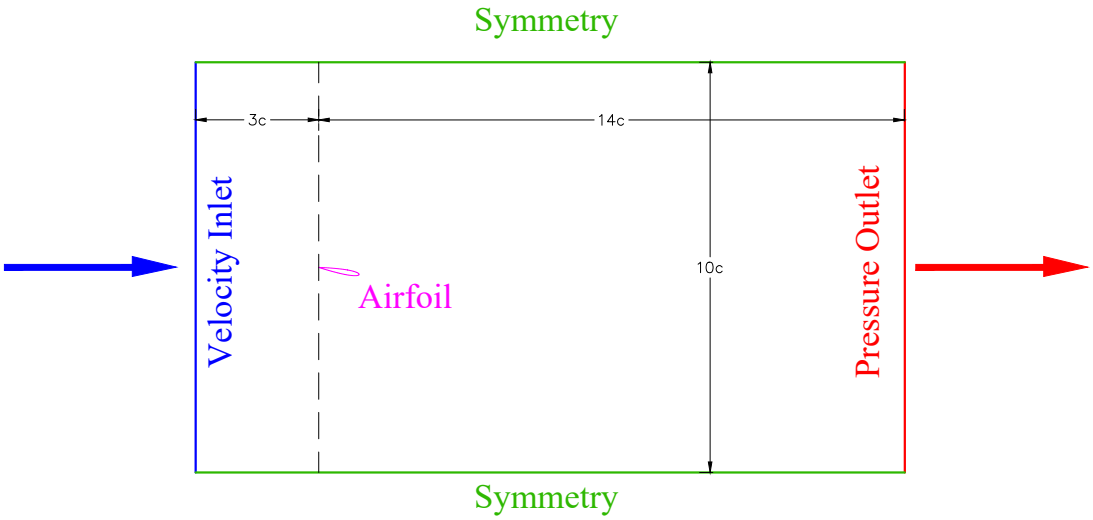

Figure 2. Computational domain.

The computational mesh was created using ANSYS ICEM software, employing a multi-block structured grid topology throughout the entire domain. This structured grid approach is well-suited for general aerodynamic applications, especially in scenarios involving laminar-to-turbulent transition [16, 17]. To achieve accurate boundary layer resolution, the entire block was subdivided to form a dedicated boundary layer block around the airfoil. The height of this boundary layer block was set to one-fifth of the chord length, allowing for a smooth transition to all adjacent outer blocks. Near the airfoil surface, the height of the first cell was set to 4×10^{-6} m, ensuring that the obtained y^+ value remained below unity for the given Reynolds number across all simulated angles of attack. Figure 3 presents the generated grid architecture near the airfoil for $\alpha = 4°$.

A grid sensitivity analysis was performed at an angle of attack of $\alpha = 10°$ to ensure a grid-independent solution. This angle was selected due to the presence of relatively high gradients in flow variables, making it a suitable test case for assessing grid convergence. The analysis involved three levels of grid refinement, and the meshing parameters are summarized in Table 3. As the numerical difference between the medium and fine grids was found to be less than 1%, the medium grid was chosen for further simulations to minimize computational cost while maintaining accuracy. The pressure-based solver is utilized to perform the computations, employing the SIMPLE algorithm for pressure-velocity coupling. Discretizations of the convective, diffusive, and transient terms are carried out using the second-order upwind scheme, while gradients are calculated with the least squares cell-based method. The turbulence closure was achieved using the algebraic SST transition model proposed by Menter et al. [18], which incorporates algebraic modifications to the original $k-\omega$ SST turbulence model to account for laminar to turbulent transition. The effectiveness of this turbulence model for reverse flow simulations was previously demonstrated by Orabi et al. [15]. In the present study, all numerical simulations were carried out using a fixed time step of 5×10^{-5} seconds. This time step was chosen to ensure temporal accuracy and stability of the computational solution while capturing the unsteady aerodynamic phenomena with sufficient resolution.

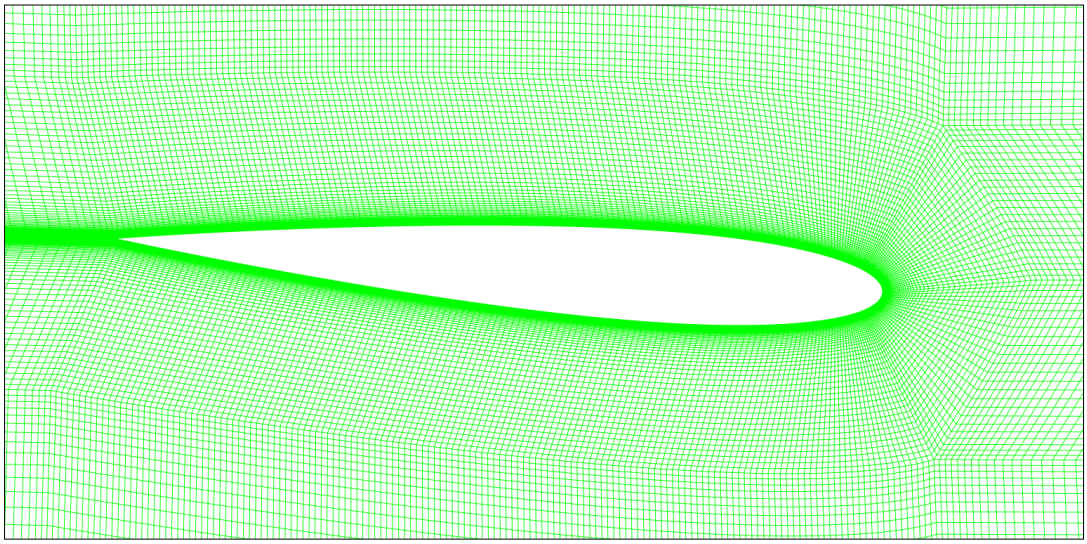

Figure 3. Structured mesh architecture ($\alpha = 4°$).

Table 3. Details of sensitivity analysis mesh parameters.

Mesh	Number of nodes along each airfoil side	Boundary layer block wall-normal direction		Outer blocks number of nodes			Total number of cells	Obtained results	
		Number of nodes	Expansion ratio	up wind	down wind	cross flow		C_L	C_D
Coarse	110	50	1.15	35	85	35	34095	0.6658	0.13
Medium	175	70	1.1	50	120	50	67414	0.6435	0.122
Fine	405	120	1.05	85	200	75	229684	0.6382	0.1212

Figure 4 presents the validation results obtained from numerical simulations across a wide range of angles of attack. The fully turbulent SST turbulence model significantly underpredicts both lift and drag forces compared to the algebraic transition model. On the other hand, the algebraic transition model shows better agreement with experimental data in the linear curve regime. Beyond this regime, the differences become more pronounced as the angle of attack increases. This comparison highlights the accuracy of the optimized computational procedures in capturing the aerodynamic behavior under reversed flow conditions.

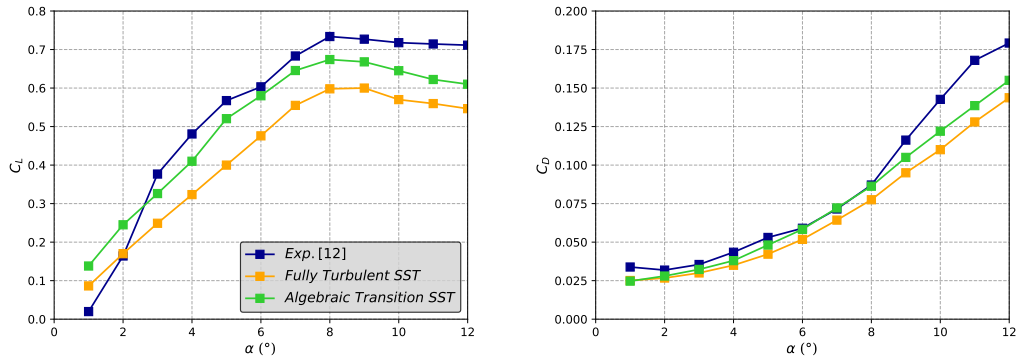

(a) Lift coefficient (b) Drag coefficient

Figure 4. Computational validation results.

5. Results and Discussion

The resultant aerodynamic forces for the current angles of attack at different stations are presented in terms of lift and drag coefficients, as shown in Figure 5.For all present angles of attack, the results show that the obtained lift forces at the mid-span station (r/R=0.5) decrease by a constant value of less than 2%, while the increase in drag is approximately 2.5% compared to the inboard station located at (r/R=0.25). However, as the rotor blade tip is approached, the scenario changes significantly for $\alpha = 4°$ and $\alpha = 6°$. The predicted decrease in lift reaches 15.5% and 10% for $\alpha = 4°$ and $\alpha = 6°$, respectively, compared to the inboard station (r/R=0.25). Meanwhile, the increase in drag reaches 30% and 11.5% for $\alpha = 4°$ and $\alpha = 6°$, respectively. At a higher angle of attack ($\alpha = 8°$), the decrease in lift is less than 5%, while the drag increases by 4.5%.

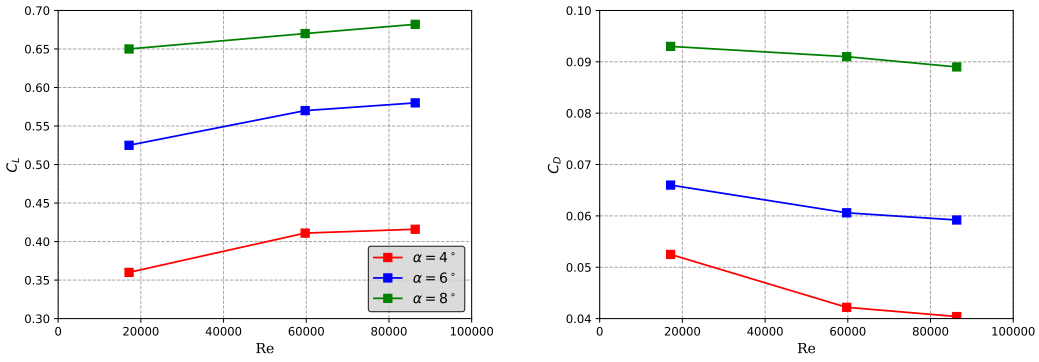

(a) Lift coefficient (b) Drag coefficient

Figure 5. NACA 0012 airfoil at different reverse flow conditions.

Surface pressure coefficients on the airfoil pressure side are plotted for all simulations. The results indicate that, regardless of the angle of attack, the surface pressure coefficients at the rotor quarter and mid-span stations remain identical. However, a noticeable decrease occurs at the tip station, becoming increasingly significant for lower angles of attack. This concludes that, as the angle of attack increases, the loss of lift caused by lower pressure on the pressure side of the airfoil becomes less sensitive to variations in the Reynolds number. Figure 6 represents the obtained surface pressure coefficients for all stations.

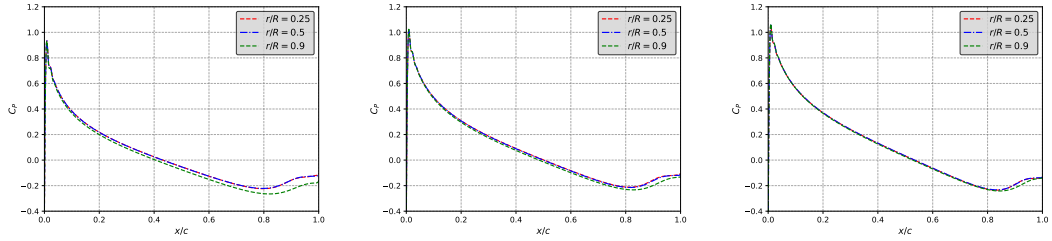

(a) Pressure side C_P at $\alpha = 4°$. (b) Pressure side C_P at $\alpha = 6°$. (c) Pressure side C_P at $\alpha = 8°$.

Figure 6. Pressure side C_P for different angles of attack.

The skin friction coefficient is defined as the ratio of wall shear stress to free-stream dynamic pressure, representing the viscous resistance generated within the boundary layer as air flows over a solid surface. Within the boundary layer, the wall shear stress decreases and eventually vanishes at separation points and locations where the flow direction reverses [19]. This phenomenon can typically be utilized to identify the onset of separation and the locations of flow reattachment. Figure 7 presents the obtained skin friction coefficient for all simulated cases. For all simulated angles of attack, a noticeable increase in the skin friction coefficient is observed at the tip station, while the difference at the rotor quarter and mid-span stations remains minor. As the flow separates upon reaching the airfoil geometric sharp trailing edge, the first minimum C_F value indicates flow reattachment. For $\alpha = 4°$, reattachment occurs at $x/c \approx 0.18$. This location remains nearly constant across all radial positions, resulting in a consistent extent of the laminar separation bubble. The fluctuations before this location are due to the circulation dynamics inside the laminar separation bubble. The second minimum C_F value indicates turbulent separation at $x/c \approx 0.92$, which is also consistent across all radial stations on the rotor retreating blade.

At a higher angle of attack ($\alpha = 6°$), the plateau exhibits a slight variation. The first minimum C_F value occurs at the rotor quarter and mid-span stations at $x/c \approx 0.08$ and $x/c \approx 0.06$, respectively, indicating the formation of a tiny separation bubble. This is followed by a second minimum C_F value at $x/c \approx 0.35$ and $x/c \approx 0.32$, respectively. The high unsteady flow circulation within these tiny bubbles can be clearly observed from the suction-side pressure coefficient distribution, as shown in Figure 8. For the tip station, reattachment of the separated bubble occurs at $x/c \approx 0.31$, with no indication of smaller bubbles.

For $\alpha = 8°$, reattachment occurs at an approximately constant location of $x/c \approx 0.56$ for all radial stations, while the flow exhibits reduced unsteadiness.

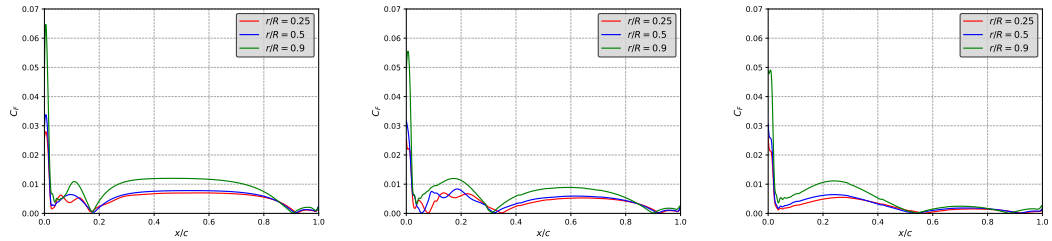

(a) Suction side C_F at $\alpha = 4°$. (b) Suction side C_F at $\alpha = 6°$. (c) Suction side C_F at $\alpha = 8°$.

Figure 7. Suction side C_F for different angles of attack.

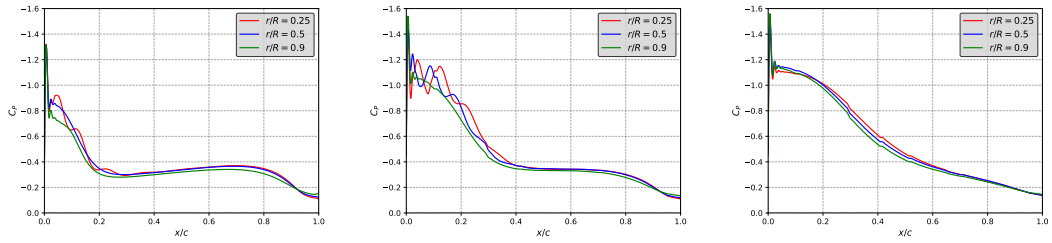

(a) Suction side C_P at $\alpha = 4°$. (b) Suction side C_P at $\alpha = 6°$. (c) Suction side C_P at $\alpha = 8°$.

Figure 8. Suction side C_P for different angles of attack.

The obtained contour results provide a detailed visualization of the flow characteristics around the rotor blade sections. These contours illustrate key aerodynamic parameters, such as velocity fields and pressure distribution, under various conditions. Figure 9 shows the stream-wise velocity contours. For $\alpha = 6°$, the dark blue spots indicate the formation of tiny separation bubbles at the rotor quarter and mid-span stations. To enhance the visibility of small-scale distributions, the contour scale limits were optimized individually for each angle of attack.

Figure 10 offers valuable insights into flow separation, reattachment, and turbulence development, providing a comprehensive understanding of the flow phenomena involved. Figure 11 presents the corresponding static contours for all cases.

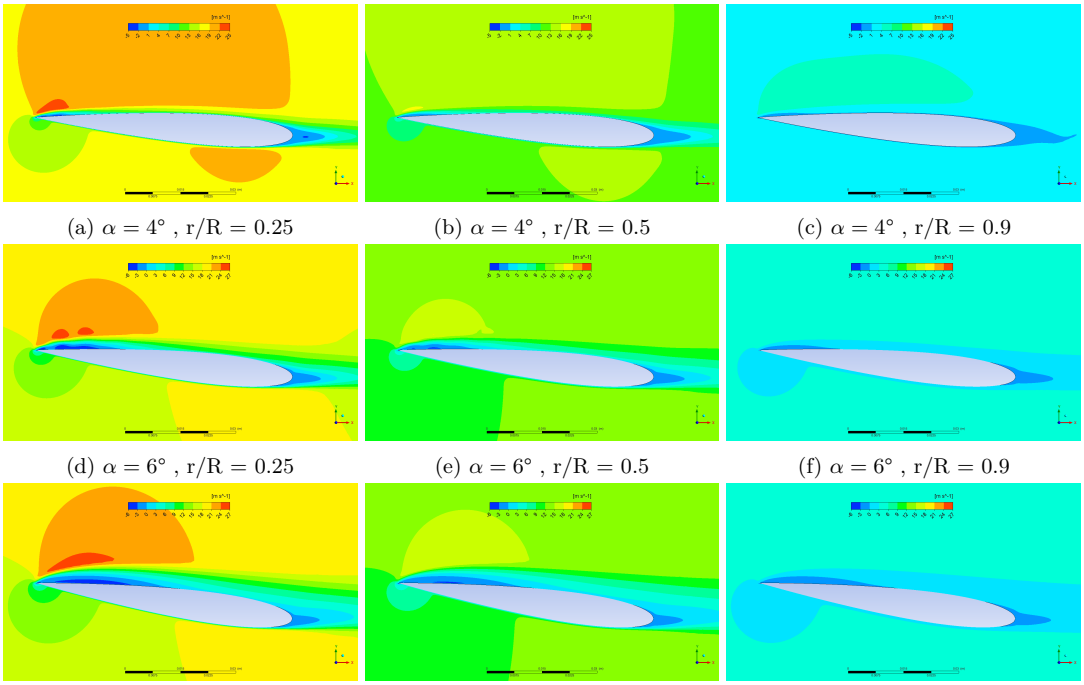

(a) $\alpha = 4°$, r/R = 0.25 (b) $\alpha = 4°$, r/R = 0.5 (c) $\alpha = 4°$, r/R = 0.9

(d) $\alpha = 6°$, r/R = 0.25 (e) $\alpha = 6°$, r/R = 0.5 (f) $\alpha = 6°$, r/R = 0.9

(g) $\alpha = 8°$, r/R = 0.25 (h) $\alpha = 8°$, r/R = 0.5 (i) $\alpha = 8°$, r/R = 0.9

Figure 9. stream-wise velocity contours.

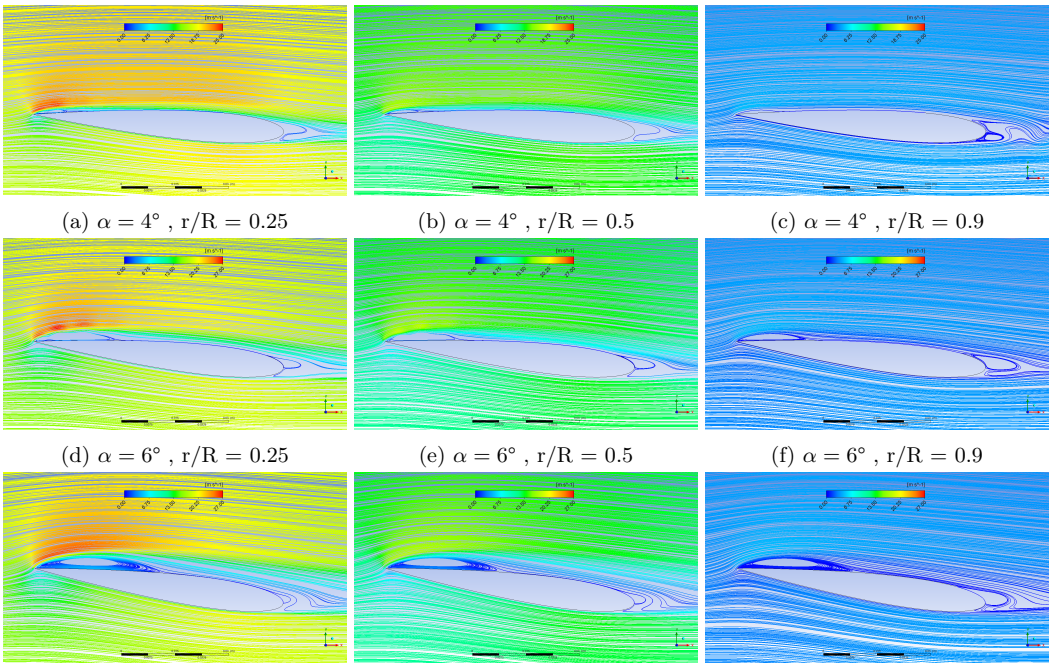

(a) $\alpha = 4°$, r/R = 0.25 (b) $\alpha = 4°$, r/R = 0.5 (c) $\alpha = 4°$, r/R = 0.9

(d) $\alpha = 6°$, r/R = 0.25 (e) $\alpha = 6°$, r/R = 0.5 (f) $\alpha = 6°$, r/R = 0.9

(g) $\alpha = 8°$, r/R = 0.25 (h) $\alpha = 8°$, r/R = 0.5 (i) $\alpha = 8°$, r/R = 0.9

Figure 10. Velocity streamlines contours.

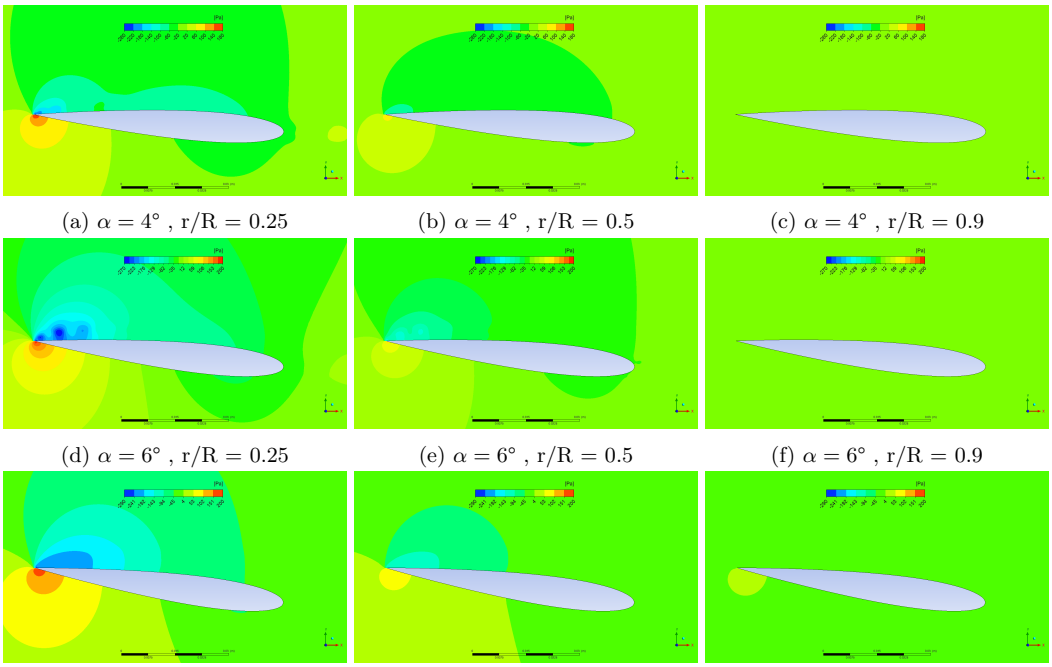

(a) $\alpha = 4°$, r/R = 0.25 (b) $\alpha = 4°$, r/R = 0.5 (c) $\alpha = 4°$, r/R = 0.9

(d) $\alpha = 6°$, r/R = 0.25 (e) $\alpha = 6°$, r/R = 0.5 (f) $\alpha = 6°$, r/R = 0.9

(g) $\alpha = 8°$, r/R = 0.25 (h) $\alpha = 8°$, r/R = 0.5 (i) $\alpha = 8°$, r/R = 0.9

Figure 11. Static pressure contours.

6. Conclusions

This study provides a numerical analysis of the aerodynamic behavior of reversed flow over rotor blade sections in a small helicopter UAV. Using a high-fidelity CFD approach based on URANS equations with algebraic transition turbulence modeling, the analysis captures key aerodynamic forces and flow characteristics under reversed flow conditions. The findings highlight the influence of the Reynolds number on reversed flow aerodynamics and compare the performance for different angles of attack. Results indicate that while the reduction in lift at the quarter and half-span is minor, a significant loss in lift and an increase in drag occur near the blade tip. These insights emphasize the need for well-designed rotors in high-speed forward flight to prevent operating at high advance ratios, where reverse flow extends across the entire retreating blade length.

This study suggests that future work should focus on employing full-rotor simulations to account for rotational flow effects in the reversed flow regime.

7. Acknowledgments

The authors would like to express their sincere gratitude to Professor Mahmoud Ahmed and Assistant Professor A. M. Kamal for their valuable academic contributions to this research. Their insightful feedback, critical discussions, and guidance throughout the course of this work have been instrumental in shaping the direction and depth of the study.

References

[1] J.Leishman. *Principles of helicopter aerodynamics*. Cambridge University Press, Second Edition, 2006.

[2] Abdallah Dayhoum, Mohamed Y Zakaria, AM Elshabka, and OE Abdelhamid. Speculation of local aerodynamic loads on helicopter rotor blade in forward flight. In *IOP Conference Series: Materials Science and Engineering*, volume 610, page 012099. IOP Publishing, 2019.

[3] Abdallah Dayhoum, Mohamed Y Zakaria, and Omar E Abdelhamid. Unsteady aerodynamic modeling and analysis of load distribution for helicopter rotor blades. *Journal of Aerospace Engineering*, 35(1):04021106, 2022.

[4] Abdallah Dayhoum, Mohamed Y Zakaria, and Omar E Abdelhamid. Experimental investigation for a small helicopter in hovering and forward flight regimes. *Journal of Aerospace Engineering*, 36(4):06023001, 2023.

[5] Amr Mansour, Mohammed Kassem, AM Abdel-Rahman, and Mohamed Y Zakaria. Aerodynamic and structural design procedures supported by fabrication and flight testing of a small unmanned helicopter. *Unmanned Systems*, pages 1–28, 2024.

[6] R. E. Sheldahl and P. C. Klimas. Aerodynamic characteristics of seven symmetrical airfoil sections through 180-degree angle of attack for use in aerodynamic analysis of vertical axis wind turbines. Technical report, Sandia National Labs., Rept. SAND80-2114, 1981.

[7] Chris C Critzos, Harry H Heyson, and Robert W Boswinkle Jr. Aerodynamic characteristics of naca 0012 airfoil section at angles of attack from 0 degrees to 180 degrees. Technical report, NACA TN-3361, 1955.

[8] Alan Pope. *The forces and pressures over an naca 0015 airfoil through 180 degrees angle of attack*. Georgia Institute of Technology, 1947.

[9] JG Leishman. Aerodynamic characteristics of a helicopter rotor airfoil as affected by simulated ballistic damage. *U. S army research lab report*, 1993.

[10] Ashish Bagai. Aerodynamic design of the x2 technology demonstrator™ main rotor blade. In *Annual forum proceedings-American Helicopter Society*, volume 64, page 29. American Helicopter Society, INC, 2008.

[11] Andrew H Lind, Jonathan N Lefebvre, and Anya R Jones. Experimental investigation of reverse flow over sharp and blunt trailing edge airfoils. In *31st AIAA Applied Aerodynamics Conference*, page 3036, 2013.

[12] Andrew H Lind, Jonathan N Lefebvre, and Anya R Jones. Time-averaged aerodynamics of sharp and blunt trailing-edge static airfoils in reverse flow. *AIAA journal*, 52(12):2751–2764, 2014.

[13] Andrew H Lind, Luke R Smith, Joseph I Milluzzo, and Anya R Jones. Reynolds number effects on rotor blade sections in reverse flow. *Journal of Aircraft*, 53(5):1248–1260, 2016.

[14] Nandeesh Hiremath, Dhwanil Shukla, and Narayanan Komerath. Vortical lift on retreating rotor blades at high advance ratios: The aerodynamics of the sharp edge vortex. *Experiments in Fluids*, 60:1–17, 2019.

[15] Mohanad Y Orabi, Mohamed Y Zakaria, Ashraf M Kamal, Mahmoud Y Ahmed, and Haithem E Taha. Computational simulations of naca 0012 in a reversed flow. In *AIAA SCITECH 2025 Forum*, 2025-2742.

[16] Krishna Zore, Alexey Matyushenko, Shoaib Shah, Cristhian Aliaga, John Stokes, and Florian Menter. Laminar-turbulent transition prediction on industrial cfd applications. In *AIAA SCITECH 2022 Forum*, page 1954, 2022.

[17] Krishna Zore, Alexey Matyushenko, Shoaib Shah, Cristhian Aliaga, John Stokes, and Florian Menter. Laminar–turbulent transition prediction on industrial computational fluid dynamics applications. *Journal of Aircraft*, 60(1):1–20, 2023.

[18] Florian R Menter, Alexey Matyushenko, Richard Lechner, Andrey Stabnikov, and Andrey Garbaruk. An algebraic lctm model for laminar–turbulent transition prediction. *Flow, Turbulence and Combustion*, 109(4):841–869, 2022.

[19] Hermann Schlichting and Klaus Gersten. *Boundary layer theory*. Springer, 2016.